UDC 681.32:681.327.634

A Numerical Simulation of Unsteady Airflow in HDDs

●Masayuki Tatewaki ●Naozumi Tsuda ●Tsugito Maruyama

(Manuscript received September 21, 2001)

In this paper, using aerodynamic numerical analysis, we investigate the mechanisms causing disk flutter in hard disk drives. A computer simulation model of three stacked disks was calculated using the finite-difference method with the LES model of turbulence. As a result, secondary airflows were found to move upward and downward though the shroud gap around the outer edge of the disk. The inference from this discovery is that a phase difference of spatial pressure patterns between the top and bottom surfaces of a disk causes disk flutter.

1. Introduction

In recent years, because of the demand for mass-storage and high-speed hard disk drives, there has been increased use of high-density recording and high-speed disk rotation. This can be seen, for example, in the Allegro series of 3.5-inch high-performance hard disk drives developed by Fujitsu. However, high-speed disk rotation causes high-speed airflows in the drive, which now have considerable effect on head positioning accuracy and power consumption.

The factors affecting the positioning of the magnetic head in hard disk drives include disk vibration, called disk flutter, and vibration of the head carriage arm and suspension. Most components of disk flutter that are asynchronous with disk rotation are known to be caused by the disturbance of airflow. Moreover, the hydrodynamic force on the carriage arm and suspension is assumed to have a big effect on positioning precision. These disturbances, including spindle-bearing vibration, become non-repeatable run-out (NRRO) components that are asynchronous with rotation.

The excitation force generated by the airflow in hard disk drives affects positioning precision. This force is caused by the spatiotemporal fluctuation of pressure generated mainly by the disturbance of airflow onto the disk and arm surface. However, the mechanisms of this pressure fluctuation and subsequent generation of vibration have not been determined. Increasing rotation speeds increases power consumption loss due to air friction (windage loss). The bulk of the power consumed by a hard disk drive is composed of the windage loss and mechanical loss of power at the shaft bearing.

Several studies of the hydrodynamic effects on the disks and carriage arms in hard disk drives have previously been reported. Lennemann[1)] used an aluminum powder compound method to conduct a visualization experiment with rotating water streams between two disks and an experiment measuring flutter vibration to check the relationships between unsteady flow patterns around disks and disk flutter. He found that the flows between the two disks were not axisymmetric. He also found that the flows were characterized by slightly slower rotations near the

laminar central core and strong turbulent flows in the peripheral area, and that both characteristics were largely affected by shroud gaps and head positions. However, he has not reached an essential resolution of the symptoms.

Kaneko *et al.*[2] used an optical cutting method to conduct a visualization experiment with rotating water streams between two disks and an experiment measuring disk pack flutter. They reported that head arm insertion and the use of a circular rectifier plate on the disk periphery reduced flutter.

Anoda[3] performed theoretical analyses, based on the linear stability theory, on the structure and generation mechanism of flows between two rotating disks. He reported that a sudden change in the distribution of main flow speed near the outer edges of the disks caused secondary flows.

Recently, Shimizu *et al.*[4] quantitatively showed a positive correlation between the disk surface pressure amplitude and the disk flutter value as determined by a numerical simulation of unsteady airflow in hard disk drives, based on Large-Eddy Simulation. Accordingly, they proposed a design method that minimizes the pressure amplitude near the outer edges of disks.

Every geometric model in these visualization experiments and the numerical simulation used two disks. Furthermore, the model for the numerical simulation used the disk center section as a periodic boundary condition to minimize the number of calculations. Therefore, the results cannot simply be applied to a multilayer model consisting of three or more disks.

With this as the background, we performed a numerical simulation using a three-layer disk model with a shroud to evaluate the effect of flows in an axial direction. Furthermore, to clarify the relationships between disk surface pressure and disk flutter that have been a matter of conjecture, we performed a response analysis using the unsteady hydrodynamic force that was obtained as the excitation force in our numerical airflow simulation.

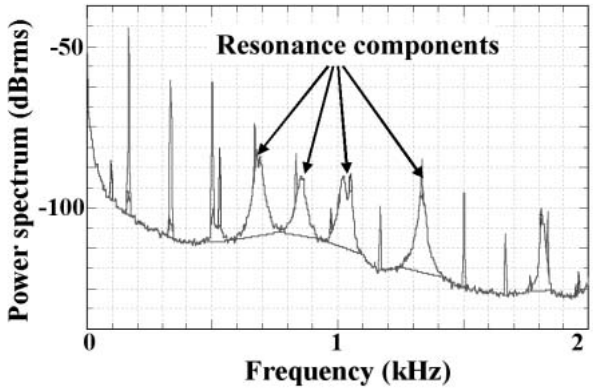

Figure 1
Power spectrum of disk flutter.

2. Fluid analysis calculation

2.1 Objective

In Fujitsu's Allegro series of 3.5-inch high-performance hard disk drives, a fundamental component of the position error signal (PES) is disk flutter. Izumi *et al.*[5] proved experimentally that the disk flutter appears as PES and is in proportion to the deflection angle of the disk. On the other hand, it is thought that the disk flutter is caused by the fluid vibration power generated by the airflow turbulence from the high-speed-rotation disk. Therefore, it is expected that PES can be decreased drastically by reducing the disk vibration power in the resonance frequency band due to the fluid.

We assembled an experimental model with the same disk diameter, same disk rotation speed, and same disk gap as one of the Allegro hard disk drives and then measured the disk flutter amplitude using a laser doppler vibrometer. **Figure 1** shows the results. In this figure, the broad peaks between 500 and 1000 Hz are the resonance components of the disk flutter. We then simulated the disk flutter of the experimental model based on the results of a numerical fluid analysis and compared the results with the measured ones.

2.2 Targets

To minimize the number of calculations, con-

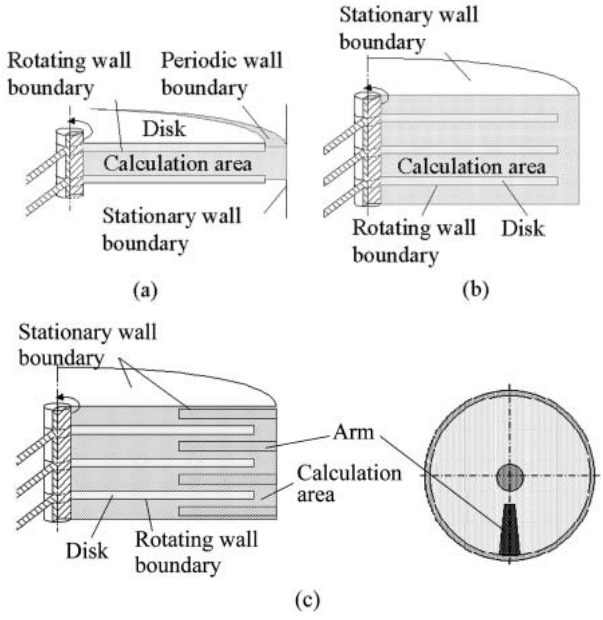

Figure 2
Comparison of calculation models.

ventional models take a portion between just two disks as the calculation area and the top-bottom surface boundary as a periodic boundary (**Figure 2 (a)**). However, since the periodic boundary condition forces the spatial wavelength of the axial flows to be less than the distance between two disks, correct flows in the axial direction cannot be obtained.

Therefore, instead of using the periodic boundary, we used a three-layer disk model as the analysis target to check the effect of flows in the axial direction (**Figure 2 (b)**).

Furthermore, to check the effect of arm insertion, we performed an analysis using arms and a shroud that surrounded the disks (**Figure 2 (c)**).

2.3 Calculation method

We used commercial fluid analysis software for the fluid analysis code. This software uses the finite volume method for the discretization method of basic equations. Here, we show a two-dimensional case to make the equations easy to understand. This method uses a basic expression that represents the Navier-Stokes equation of motion and the equation of continuity (the law of conservation of mass) as an integral form [Equation (1)] and differentiates it for discretization [Equation (2)]. In these equations, t is the time, Ω is the control volume, V is the volume, $\vec{A}$ is the unit normal vector of the control surface of the cell boundary, and ρ is the density of the air. Also, u and v are the flow velocities in the x and y directions, respectively, p is the pressure, e is the internal energy per unit volume, n is the discrete time, and i and j are the grid numbers.

Table 1
Calculation methods.

Item	Calculation method
Basic equation	3-dimensional Navier-Stokes equation
Spatial discretization	2nd-order finite-volume method (FVM)
Time advancement	Unsteady (2nd-order implicit method)
Turbulence model	Large-Eddy Simulation (LES)

A time series of flow velocities and pressures at each grid point is obtained by calculating Equation (2) iteratively.

$$\frac{\partial}{\partial t}\int_{\Omega}\mathbf{Q}dV + \int_{\partial\Omega}\mathbf{H}\cdot d\vec{A} = 0 \qquad (1)$$

where

$$\mathbf{H} = (\mathbf{E}, \mathbf{F})$$

$$\mathbf{Q} = \begin{bmatrix}\rho\\ \rho u\\ \rho v\\ e\end{bmatrix},\ \mathbf{E} = \begin{bmatrix}\rho u\\ p+\rho u^2\\ \rho vu\\ (e+p)u\end{bmatrix},\ \mathbf{F} = \begin{bmatrix}\rho v\\ \rho vu\\ p+\rho v^2\\ (e+p)v\end{bmatrix}$$

$$\mathbf{Q}_{j,k}^{n+1} = \mathbf{Q}_{j,k}^{n} - \Delta t\cdot\left[\frac{\mathbf{E}_{j+1,k}^{n} - \mathbf{E}_{j-1,k}^{n}}{2\Delta x} + \frac{\mathbf{F}_{j,k+1}^{n} - \mathbf{F}_{j,k-1}^{n}}{2\Delta y}\right] \qquad (2)$$

The Large-Eddy Simulation model was used for calculating turbulent flows. This method features a level of precision in its unsteady analysis results that is higher than that obtainable with such Reynolds mean models as the κ-ε model. **Table 1** summarizes the calculation methods used for our unsteady fluid analysis.

2.4 Analysis conditions and grid models

The disk rotation speed was 10 000 rpm, which is similar to the speed in commercial hard disk drives. The disk diameter was 3.3 inches.

Table 2
Analysis conditions.

Item	Value
Number of disks	3
Disk diameter, Dd (inch)	3.3
Disk rotation speed, ω (rpm)	10 000
Disk thickness (mm)	0.8
Shroud gap, δ (mm)	2
Disk gap, G (mm)	1.84
Time step, Δt (ms)	0.1
Turbulence model constant, Cs	0.1

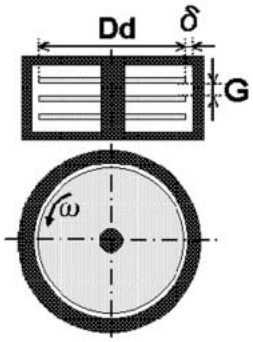

Figure 3
Model parameters.

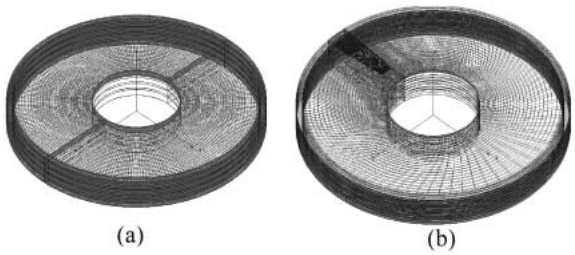

Figure 4
Grid models.

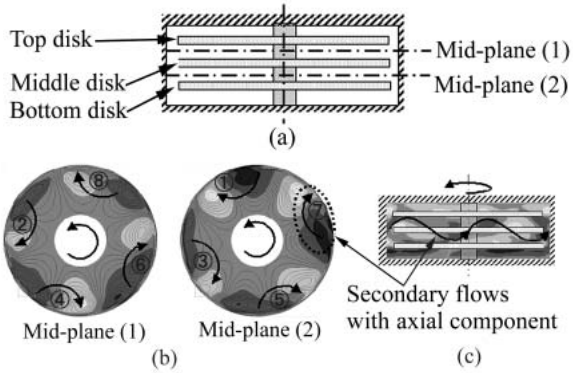

Figure 5
Airflow pattern without arms.

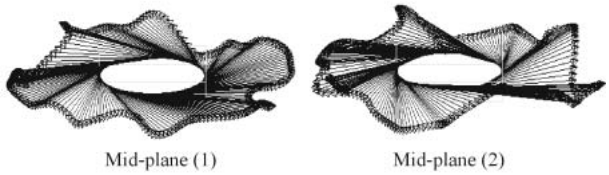

Figure 6
Flow velocity vectors in the shroud gap.

The shroud gap was set to 2 mm to observe secondary flows more easily. The time step for unsteady calculation was set to 0.1 ms to detect vibrations of up to 5 kHz. The turbulence model constant was set to 0.1 as the most general value. **Table 2** lists the analysis conditions used for our study, and **Figure 3** shows their parameter values.

Figure 4 shows the grid models for the fluid analysis. Figure 4 (a) shows the model without arms, and Figure 4 (b) shows the model with arms.

2.5 Analysis results

In this section, we describe the results of the fluid analysis.

2.5.1 Flow pattern without arms

First, we observed the flow fields in the drive.

Figure 5 (b) shows the contours of flow velocities of a radial component on the mid-plane of the disks. This figure shows the existence of secondary flows caused by large-scale vortices generated around the disks. **Figure 5 (c)** shows the contours of flow velocities in the axial direction.

Figure 6 shows flow velocity vectors at a certain radial position in the shroud gap. The directions of these vectors follow the perimeter, and it is understood that they alternate in the up-down direction.

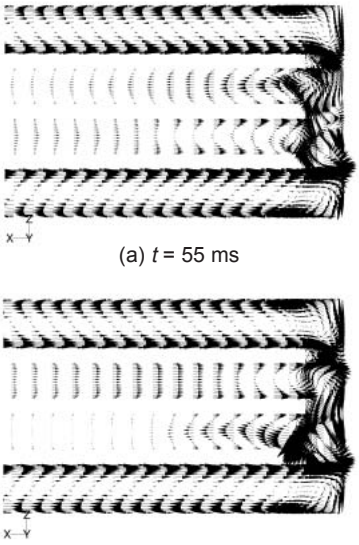

(a) t = 55 ms

(b) t = 70 ms

Figure 7
Flow velocity vectors in an r-z section.

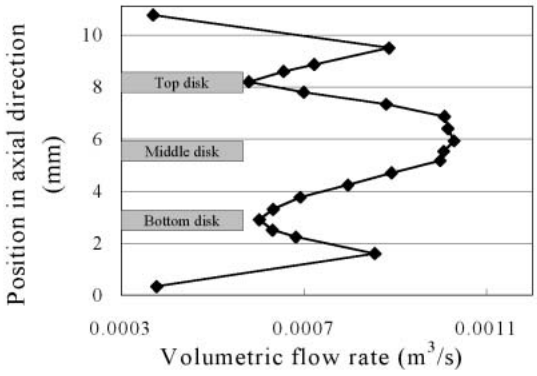

Figure 8
Flow rate in axial direction in the shroud gap.

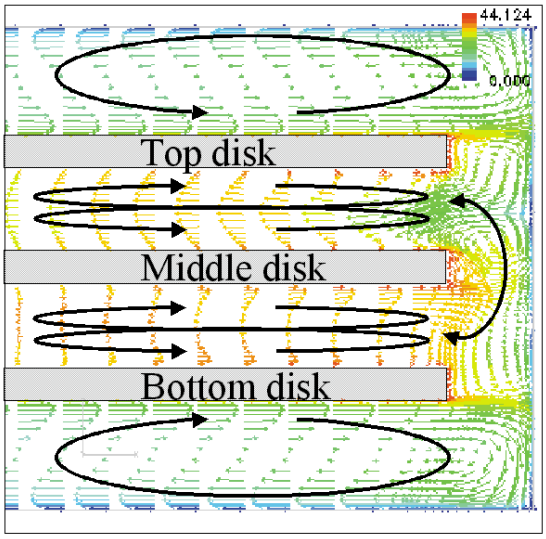

Figure 9
Pattern diagram of flows.

Figure 7 shows flow velocity vectors in an r-z section at circumferential position θ. Figure 7 (a) shows the vectors at time t = 55 ms, and Figure 7 (b) shows the vectors at time t = 70 ms. Furthermore, centrifugal forces produce large-scale vortices in the θ direction in the top/bottom disk-casing space and twin large-scale vortices are seen in the gaps between the middle disk and the top and bottom disks.

Figure 8 shows the tempospatial mean volumetric flow rate in the axial direction in the shroud gap. This graph shows that axial flows between the top and bottom spaces of the middle disk are dominant in the shroud gap, while those of the top and bottom disk are small.

Figures 7 and 8 suggest that the flow pattern in the r-z section is composed of the two basic flows shown in **Figure 9**. One is a core flow caused by centrifugal forces in the gap between disks, and the other is a secondary flow vibrating in the axial direction through the shroud gap around the disk circumference area.

These figures demonstrate that secondary flows move upward and downward in an axial direction through the shroud gap around the disk periphery. The path order of the secondary flows is indicated in Figure 4 by the numbers around the disks.

This result has not been observed in conventional models, and for the first time in the industry we have found secondary flows with an axial component.

2.5.2 *Comparison with the results of previous researches*

As shown in Figure 5, the number of large-scale vortices indicates that the secondary flow is in flow mode 4, where the "flow mode" refers to the polygonal shape of the core region. With reference to the experimental results of Lennemann

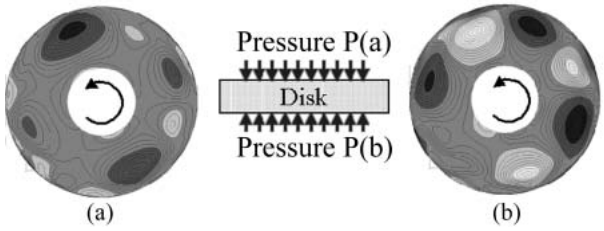

Figure 10
Pressure difference without arms.

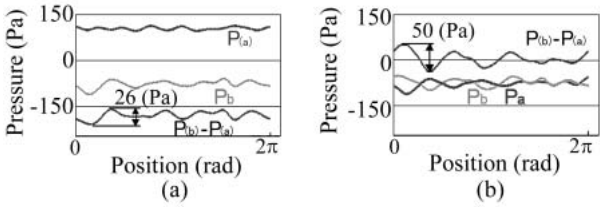

Figure 11
Profile of pressure difference on disks.

and Funaki,[6] our model (rotation Reynolds number Re = 1.2×10^5, dimensionless shroud gap λ = 0.048, and dimensionless disk gap δ = 0.034) was assumed to be in flow mode 6 or 7. The following is a possible reason why the secondary flow mode number is as low as mode 4. Lennemann and Funaki used a model that had an airtight gap between the outer edge of the disk and a shroud wall with protuberances, but we used a model that had a wide gap with a flat shroud wall. Therefore, the secondary flow also had a flow structure in the axial direction and the vortex scale becomes large.

2.5.3 Pressure difference without arms

We observed the fluid force fields as pressure differences on each disk.

Figure 10 shows the contours of the pressure difference without arms between the top and bottom surfaces of each disk. Due to axial flows through the shroud gap, the pressure on the middle disk produces pressure space contours where the phase shifts by 180 degrees between the top and bottom surfaces.

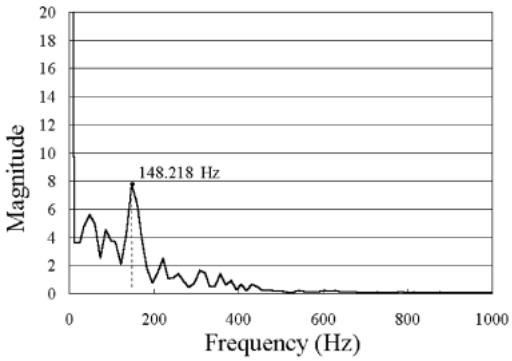

Figure 12
Frequency analysis result.

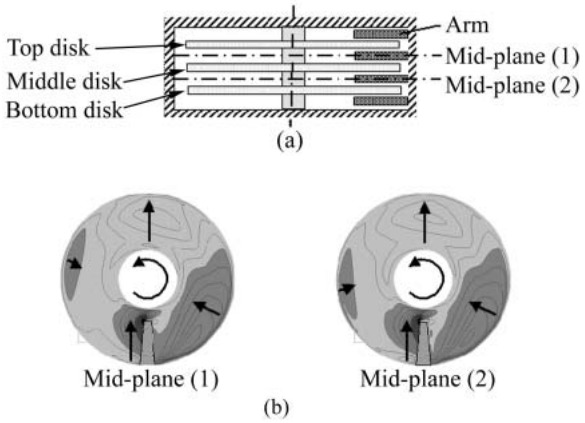

Figure 13
Airflow pattern with arms inserted.

Therefore, on the middle disk, the pressure difference is about 1.9 times larger than that on the top and bottom disks (**Figure 11**).

In the frequency analysis result of time series pressure differences acting on the middle disk, the peak frequency of 148.2 Hz reveals that the secondary flow rotates at 2964 rpm (**Figure 12**).

2.5.4 Flow pattern with arms inserted

We examined the effect of the arms in terms of aerodynamics.

Figure 13 (b) shows the contours of flow velocities of the radial component on the mid-plane of disks in the model with the arms inserted. The secondary flow generated around the disks in the model without arms is not seen in this model.

As a result, the arms rectify secondary flow turbulence.

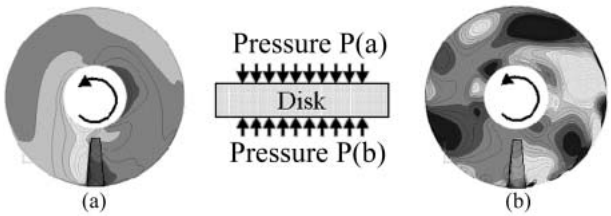

Figure 14
Pressure difference with arm inserted.

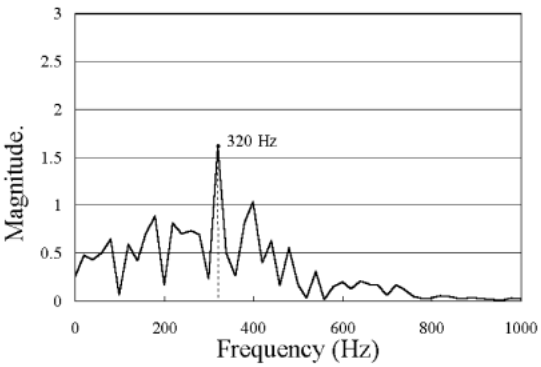

Figure 15
Frequency analysis result with arms inserted.

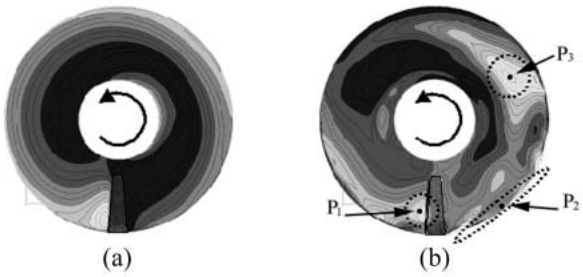

Figure 16
Excitation forces with arms inserted.

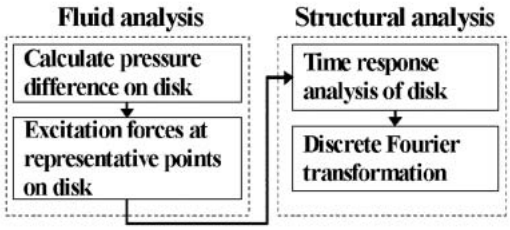

Figure 17
Analysis procedure.

2.5.5 *Pressure difference with arms inserted*

We observed the fluid force fields in the model with the arms inserted. **Figure 14** shows the contours of the pressure difference between the top and bottom surfaces of each disk with the arms inserted.

On the middle disk (Figure 14 (b)), spatial fluctuations along the outer circumference of the disk are observed.

Figure 15 shows a frequency analysis of time series pressure differences on the middle disk. The peak frequency is 320 Hz. This frequency is higher than that of the model without arms, so it is reasonable to assume that arm insertion increases the flow velocity.

2.5.6 *Excitation forces on disks with arms inserted*

We observed the excitation force fields. The excitation forces F were computed by Equation (3).

$$F = \sqrt{\frac{1}{T}\sum_t \left[\left(P_b(t) - P_a(t)\right) - \frac{1}{T}\sum_t \left(P_b(t) - P_a(t)\right)\right]^2} \qquad (3)$$

From these contours, on the top disk, the only significant excitation area is the area near the arm. On the middle disk, there are three dominant excitation areas. The first is near the arm, the second is the downstream outer circumference of the arm, and the third is the downward reach of the arm. In **Figure 16**, P1, P2, and P3 are representative points of each excitation force area.

3. Structural analysis calculation

3.1 Time response analysis procedure

Based on the time series pressure values obtained by fluid analysis, we performed a time response analysis of disk flutter using the finite element method. The analysis procedure is shown in **Figure 17**.

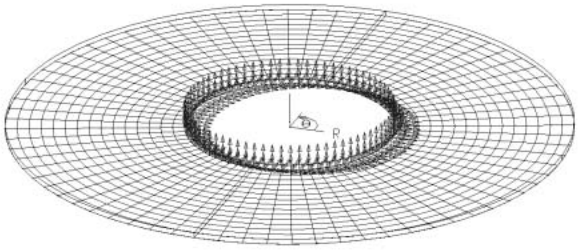

Figure 18
Finite element model.

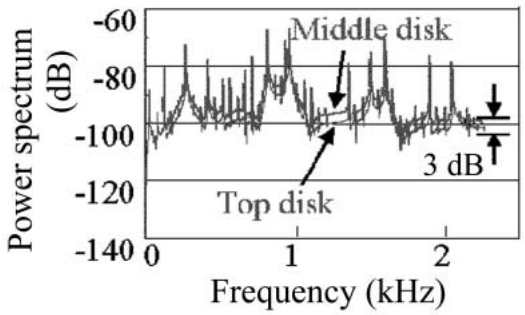

Figure 19
Time response analysis results displayed as a power spectrum format.

First, the pressure difference acting on each disk at a certain moment was obtained. Excitation forces on disks based on pressure differences are represented by concentrated forces at the representative point. In the case with arms inserted, the representative points in Figure 16 are P1, P2, and P3. The amplitude of the concentrated force was determined by the areal integration of the pressure difference for each area. In Figure 16, P1, P2, and P3 represent the concentrated force.

The disk flutter amplitude determined from the response analysis was converted into spectra by discrete Fourier transformation.

3.2 Finite element model

Figure 18 shows the finite element model used to perform a structural analysis. It is composed of thin shell elements. The inside periphery is clamped at 6 degrees of freedom.

3.3 Comparison with experimental results

Figure 19 shows the time response analysis results. The amplitude of the power spectrum of the middle disk is about 3 dB greater than that of the top disk (**Table 3**). The results in Figure 19 match the pattern found in non-repeatable runout measurements done on commercial hard disk drives, which supports our simulations and the results we obtained.

Table 3
Experimental results.

Disk position	NRRO (Resonance component)
Top	0.119 μm
Middle	0.184 μm

4. Conclusions

An unsteady fluid analysis using a three-layer disk model demonstrated that secondary flows move upward and downward in an axial direction through the shroud gap.

An analysis carried out via simulations revealed that a three-layer disk drive with arms inserted has more disk flutter on the middle disk than on the top and bottom disks. The results of a time response analysis we performed on rotating disks matched the experimental results.

References

1) E. Lennemann: Aerodynamic Aspects of Disk Files. *IBM. J. Res. Develop.*, p.480-488 (1974).
2) R. Kaneko, Y. Mitsuya, S. Oguchi, and K. Hoshiya: Hydrodynamic Aspects and Design of Rotating Disk Mechanism. (In Japanese), *NTT R&D*, **26-2**, p.563-583 (1977).
3) T. Anoda: Study on Non-axisymmetric Swirling Flow Generated between Parallel Rotating Disks. *JSME Int. J. Series B*, **49**, 440, p.809-817 (1983).

4) H. Shimizu, S. Imai, and K. Sakai: Improvement of Hard Disk Drives Performance by Applying Computer Aerodynamic Simulation. JSME Conference on Information, Intelligence and Precision Equipment, Tokyo, Japan, 99-13, 1999, p.25-28.
5) M. Izumi, T. Yamada, M. Yoshida, and K. Aruga: Correlation between disk flutter and head-positioning error in hard disk drives. Lecture Paper Library IV, Proceedings of the 75th Ordinary General Meeting of JSME, 1998, p.202-203.
6) J. Funaki, K. Hirata, and H. Yano: Flow Modes in Gap between Coaxial Rotating Disks. *JSME Int. J. Series B,* **61**, 588, p.2924-2929 (1995).

Masayuki Tatewaki received the B.S. and M.S. degrees in Precision Engineering from Osaka University, Suita, Japan in 1989 and 1991, respectively. He joined Fujitsu Laboratories Ltd., Kawasaki, Japan in 1991, where he has been engaged in research and development of advanced space robot testbeds with redundant arms.

Naozumi Tsuda received the B.S. and M.S. degrees in Mechanical Engineering from Gunma University, Maebashi, Japan and Tohoku University, Sendai, Japan in 1990 and 1992, respectively. He joined Fujitsu Laboratories Ltd., Kawasaki, Japan in 1992, where he has been engaged in research and development of advanced robot hand systems working in low earth orbit. He is a member of the Robotics Society of Japan (RSJ) and the Japan Society for Aeronautical and Space Sciences (JSASS).

Tsugito Maruyama received the M.E. and Dr. degrees in Electrical and Communication Engineering from Tohoku University, Sendai, Japan in 1976 and 1980, respectively. He joined Fujitsu Laboratories Ltd., Kawasaki, Japan in 1980, where he has been engaged in research and development of 3-D robot vision, a pin-insertion robot, a food-carrying robot for the aged and disabled, and high-positioning control for hard disk drives. He is a member of the Society of Instrument and Control Engineers (SICE) and the Robotics Society of Japan (RSJ).